Supramolecular Polymer Polymorphism: Spontaneous Helix-Helicoid Transition through H-to-J type Dislocation of Hydrogen-Bonded π-Rosettes

Chie Otsuka, Sho Takahashi, Atsushi Isobe, Takuho Saito, Takumi Aizawa, Ryoma Tsuchida, Shuhei Yamashita, Koji Harano, Hiroki Hanayama, Nobutaka Shimizu, Hideaki Takagi, Rie Haruki, Luzhi Liu, Martin J. Hollamby*, Takahiro Ohkubo* and Shiki Yagai*

ABSTRACT: Polymorphism, a phenomenon whereby disparate self-assembled products can be formed from identical molecules, has incited significant intrigue in the field of supramolecular polymers. Conventionally, the monomers that constitute supramolecular polymers are engineered to facilitate one-dimensional aggregation, and consequently, their polymorphism surfaces primarily when the states of assembly differ significantly. This engenders polymorphs of divergent dimensionalities, such as one-dimensional and two-dimensional aggregates. Notwithstanding, realizing supramolecular polymer polymorphism wherein polymorphs maintain one-dimensional aggregation persists as a daunting challenge. In this work, we expound upon the manifestation of two *supramolecular polymer polymorphs* formed from a large discotic supramolecular monomer (rosette), which consists of six hydrogen-bonded molecules with an extended π-conjugated core. These polymorphs are generated in mixtures of chloroform and methylcyclohexane, attributable to distinctly different disc stacking arrangements. These arrangements can be classified as H-type and J-type stacking predicated on their distinctive photophysical properties. The H-type stacking, delineated by minimal rosette displacement, results in a twisted helix structure. Conversely, the J-type stacking, characterized by significant rosette displacement, induces inherent curvature in the supramolecular fiber, thereby culminating in a hollow helical coil (helicoid). While both polymorphs exhibit bistability in nonpolar solvent compositions, the H-type stacking attains stability purely in a kinetic sense within a polar solvent composition and undergoes conversion into the J-type stacking through a dislocation of stacked rosettes. This occurs without the dissociation and nucleation of monomers, leading to an unprecedented helicoidal folding of supramolecular polymers. The direct helicoidal folding of supramolecular polymer fibers enables the transformation of extraordinarily long twisted helices into helicoids over the mesoscopic regime. Concurrently, distinct cohesive behaviors manifest in conjunction with the structural conversion observed within these extended supramolecular polymer materials. Our findings not only augment our understanding of supramolecular polymer polymorphism, but they also highlight a distinctive method for achieving helicoidal folding in supramolecular polymers.

The self-assembly of discotic molecules with extended π-conjugated systems, primarily facilitated by π–π interactions, represents a significant and appealing feature in the exploring of novel functional molecules.[1–6] Notably, the stacking arrangements of π-conjugated molecules, such as H-type or J-type, profoundly influence their photophysical and electronic properties via the electronic coupling of the π-conjugated systems.[7–10] In addition, these stacking arrangements considerably impact their material properties as exhibited in solution or bulk states, including gel formation[11,12] and mesomorphism.[13,14]

In recent years, mesoscopic one-dimensional aggregation of π-conjugated molecules in the solution phase, accomplished through thoughtful molecular design concentrated on solute-solute and solute-solvent interaction,[15] has elicited much interest as novel polymer materials, referred to as supramolecular polymers.[16–19] Unlike conventional supramolecular polymers founded on multiple hydrogen bonds or host-guest interactions,[20,21] those predicated on π-conjugated molecules can propagate the conformational order of rigid building blocks via stacking along their main chains, resulting in the formation of one-dimensional fibers with superior internal order.[18,22] Consequently, their self-assembly process presents an analogy to the formation of crystals, with the monomers initially surmounting a high energy barrier to form a template (nucleus) for a highly ordered assembly[17,23]. This self-assembly process proceeds via a cooperative mechanism comprised of nucleation and elongation processes. The resulting long-range structural ordering along the main chain of the supramolecular polymer allows the emergence of functionality-related structural properties such as helicity.[24–30]

The investigation of supramolecular polymers composed of π-conjugated molecules is indeed intriguing; however, their practical implementation necessitates the discovery of new properties that can only be realized with this material. Of late, supramolecular polymorphs and the conversion between polymorphs[31–40] have garnered specific significance as they are deeply intertwined with the physical and adaptive properties of supramolecular polymers and the kinetic aspect of supramolecular polymerization.[41–43] Unlike crystalline compounds, monomers that form supramolecular polymers have been designed to continuously interact with other molecules one-dimensionally. Consequently, the assembly states distinct from the originally designed states can exist bistably only when the conformations of the monomer differ significantly. This result in entirely different supramolecular packing structures, which would lead to a combination of assembly states with distinctly different dimensionalities and morphologies such as supramolecular polymers (1D) and sheets (2D)[32,34,44] or spheres (0D)[37,45]. Therefore, one-dimensional supramolecular polymorphs of clearly different structures and their conversions are indeed very rare.[33,46–48]

We anticipate that the manifestation of such *supramolecular polymer polymorphs* with an A→B polymorphic conversion, particularly those occurring in meso-to-macroscopic region, would bestow upon the supramolecular polymer new stimuli-responsive properties. For this purpose, the A→B polymorphic conversion must occur via a direct conformational alteration of monomer molecules for a polymer chain

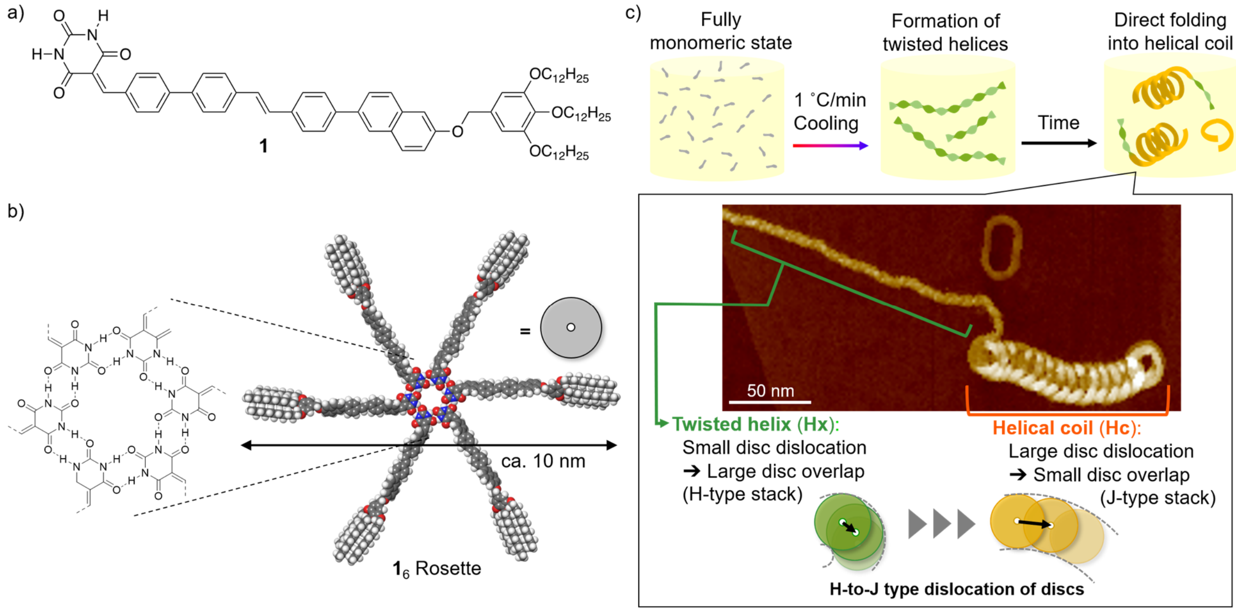

Figure 1. (a) Molecular structure of **1**. (b) Chemical structure of the barbituric acid rosette and a molecular modelled rosette of **1**. (c) Schematic representation of supramolecular polymerization of **1** and its polymorphic transition from twisted helix (**Hx**) to helical coil (**Hc**).

with sufficient length in the mesoscopic scale. Otherwise, the release of the monomer from the polymorph A and subsequent nucleation to form the polymorph B would result in a reduction of the polymer chain length.

In this study, we demonstrate that a supramolecular polymer polymorphism and a polymorphic conversion in the mesoscopic regime can be accomplished in the form of two markedly different helical structures, i.e., twisted helices and helical coils, by employing a large, star-shaped π-conjugated building block (Figure 1). The star-shaped building block, known as a rosette (hexameric supermacrocycle), is formed by hydrogen bonding of extended π-conjugated molecules with barbituric acid.[49,50] The rosette we use in this study has six π-conjugated arms that are more extended than those of similar molecules we have previously developed.[51,52] Its potent aggregation capability is evidenced by supramolecular polymerization even in good solvents such as chloroform. Notably, we observed the formation of metastable twisted helices in chloroform, which subsequently transitioned to helical coils within a span of a few hours. By utilizing a nonpolar co-solvent such as methylcyclohexane (MCH) that enhances intermolecular interactions, the supramolecular polymers were able to extend to the mesoscale, and the conformational transition was decelerated to the order of days. AFM tracing of the progression of this structural conversion revealed that it occurred directly through main chain folding, without monomer dissociation and reassembly. In solvent systems that were richer in MCH, these fibrous polymorphs could be prepared as bistable states. This enabled small angle X-ray scattering (SAXS) and spectroscopic measurements, and the ensuing structural information, in conjunction with a molecular modeling simulation, indicated that the dislocation of the rosette from H-type (small offset) to J-type (large offset) was responsible for this polymorph conversion.

RESULTS

Aggregation in Chloroform: Formation of Two Supramolecular Polymer Polymorphs. π-Conjugated molecule **1** equipped with barbituric acid at one terminus and an aliphatic wedge[53] at the other (Figure 1a) was designed in this study. The molecular design builds upon the previously reported 2,6-diphenylnaphthalene monomer **2**[51,52] (Figure S1a) known to form helically folded supramolecular polymers as a consequence of an intrinsic curvature generated through a unique stacking of rosettes with translational and rotational displacements.[54,55] Given that the intrinsic curvature was not produced when the central naphthalene core was replaced with anthracene to enhance the π–π interaction,[56] an attempt was made to introduce a stilbene moiety as the central core in the current study. Moreover, by substituting one of the phenyl groups with a naphthyl group to further expand of the π-conjugated system, we obtained the structure of **1**. Compound **1** was synthesized following the procedure delineated in the Supporting Information and was subsequently recrystallized from ethanol. Density functional theory (DFT) calculations revealed that **1** possesses a moderately high dipole moment of 7.5 D (see the Supporting Information), which is greater than that of **2** (5.9 D). This attribute may be responsible for the polymorphism of this compound.

A robust intermolecular interaction among $\mathbf{1}_6$ rosettes possessing six π-extended arms was demonstrated through their aggregation in chloroform ($CHCl_3$), commonly used as a "good solvent" for the dissolution of molecules with large π-conjugated systems.[57] The as-crystallized solid of **1** was insoluble in chloroform at room temperature due to the formation of nanostructures organized in a lamellar fashion (Figure S2). This indicates the formation of a polymorph grounded in a tapelike hydrogen-bonded pattern of the barbituric acid unit.[40,52,58–60] The crystalline solid could be dissolved in chloroform (total concentration of monomer, c_t = 300 μM) by heating just above the boiling point of chloroform (61.2 °C). During the subsequent cooling to 20 °C at a rate of 1 ˚C/min, a hypsochromic shift of the absorption maximum of **1** from 424 nm to 406 nm was observed in UV/vis measurements (Figure 2a, black dashed line to blue solid line), yielding a homogeneous solution.

Upon spin-coating the aforementioned solution onto a highly oriented pyrolytic graphite (HOPG) substrate, atomic force microscopy (AFM) revealed a substantial population of helically twisted fibers alongside toroidal structures (Figure 2b, S3a). Due to their simple helical architecture, these fibers will henceforth be denoted as **Hx** (helix). This observation underscores the strong aggregation propensity of **1**, given that a previous compound **2**, known to form curved supramolecular polymers in aliphatic solvents[51,52] presented a preponderance of ill-defined structures with minor amounts of toroids under the same AFM experiment utilizing a chloroform solution (Figure S1b). When the solution of **1** was maintained at 20 °C, time-dependent bathochromic and hyperchromic shifts of the absorption spectrum were detected over a span of hours (Figure 2a). Remarkably, AFM analysis after 90 min unveiled that most **Hx** had been converted into helically folded fibers while toroids remained unaffected (Figure 2c, S3b). Due to their distinct helical structures with helical surface, these folded fibers will hereafter be referred to as **Hc** (helicoid). The generation of toroids is a common occurrence in our curved supramolecular polymer systems, and can be rationalized as a kinetic trapping of stable ring-closed products in the preliminary stages of supramolecular polymerization.[54,55,61] Only the polymeric species that could escape from such a kinetic trap have the opportunity to further elongate, yielding helically folded supramolecular polymers as thermodynamic products.[54,55] These results suggest that the direct formation of **Hc** from monomeric **1** is impossible, and its formation is preceded by the kinetic formation of **Hx**.

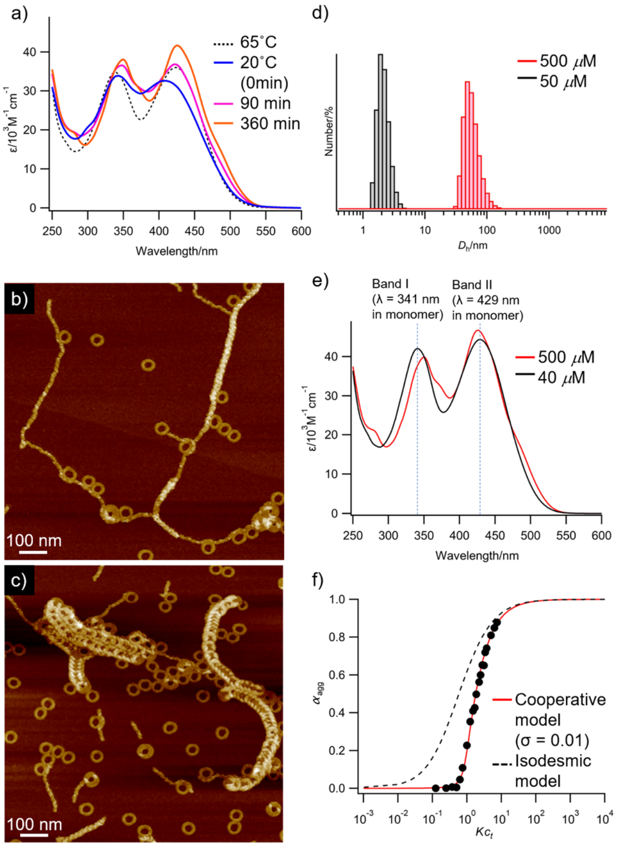

Figure 2. (a) Temperature and time-dependent absorption spectra of **1** in CHCl3 (c_t = 300 μM) upon cooling and subsequent aging for 360 min. (b,c) AFM image of the supramolecular polymers of **1** (b) formed immediately after cooling the CHCl3 solution (c_t = 300 μM) and (c) formed upon aging the solution for 90 min. The samples were prepared by spin-coating the solutions on HOPG. Larger-scale AFM images are shown in Figure S3. (d) DLS profiles of equilibrated CHCl3 solutions of **1** at c_t = 50 (black bars) and 500 μM (pink bars). (e) UV/vis absorption spectra of **1** in CHCl3 at c_t = 40 and 500 μM. (f) Fraction of aggregated molecules (α_{agg}) estimated from the absorption changes as a function of Kc_t upon diluting a c_t = 500 μM solution including **Hc** and toroids. Red solid and black dashed curves represent simulated curves according to cooperative (σ = 0.01) and isodesmic models, respectively.

As the aforementioned observations demonstrate that **Hc** is the thermodynamic product, we proceeded to assess its thermodynamic stability via concentration-dependent study. Upon diluting a thermodynamically equilibrated c_t = 500 μM CHCl3 solution containing **Hc** and toroids to 50 μM, the average hydrodynamic diameter (D_h) in dynamic light scattering (DLS) measurements diminished from 53.6 nm to approximately 2 nm (Figure 2d), suggesting the dissociation of assemblies into the monomeric state. This dilution-induced dissociation was also discernible in UV/vis measurements, wherein absorption shoulders around λ = 373 and 488 nm, associated with electronic interaction between π-conjugated chromophores, disappeared at c_t = 40 μM (Figure 2e). When the degree of aggregation (α_{agg}) estimated from the absorption spectral change was plotted against Kc_t (K being an equilibrium constant), a non-sigmoidal aggregate-to-monomer transition was observed, with the critical concentration approximating c_t = 40 μM (Figure 2f). This finding confirms that **1** undergoes supramolecular polymerization via the nucleation-elongation mechanism. The transition curve could be fitted with the cooperative $K_{nucleation}/K_{elongation}$ model[62,63] by setting the cooperative factor σ (= $K_{nucleation}/K_{elongation}$) to 0.01 and $K_{elongation}$ to 12500 M^{-1}, thereby enabling the estimation of $K_{nucleation}$ as 125 M^{-1}. The σ and K values are congruent with those of melamine-cyanurate rosette that bears three strongly-aggregating perylene bisimide dyes in chloroform.[64]

Folding of Metastable Twisted Helices into Helicoid. Although the **Hx**→**Hc** polymorph conversion in CHCl3 proceeded too rapidly to allow us a detailed study and further comparison of the physical properties of **Hx** and **Hc**, we discovered that employing nonpolar methylcyclohexane (MCH) as a co-solvent enhances the stability of **Hx** and decelerate the polymorph conversion to span over several days. This allowed us to discern the distinct physical properties of the supramolecular polymers, and furthermore, observe a direct helix-helicoidal transition without monomer release and nucleation.

Considering that the original crystalline solid of tapelike hydrogen-bonded **1** could not be directly dissolved when 30% of CHCl3 was substituted with MCH (i.e., 70:30 CHCl3/MCH mixture), we prepared a film by evaporating an equilibrated chloroform solution (c_t = 500 μM) containing **Hc** and toroids. This supramolecular polymer film was easily dissolved in 70:30 CHCl3/MCH mixture (c_t = 50 μM) by heating to 100 °C in a 1.0-cm path-length quartz cuvette. Upon cooling the heated solution to 25 °C at 1 °C/min without stirring, we observed the adhesion of film-like materials to the inner walls of the cuvette. AFM indicated that the solution phase contained only **Hx** (Figure S4). Analogous to the cooling in a CHCl3 solution, a hypsochromic shift of the absorption maximum of **1** from 416 nm to 389 nm was observed, attributable to the formation of **Hx**. Despite the substantial fraction of CHCl3 (70%) in the solvent mixture, the absorption spectrum of the solution remained unchanged (Figure S5), and no **Hx**→**Hc** polymorph conversion was confirmed by AFM upon leaving this heterogeneous sample undisturbed for one week. It is noteworthy that the emission color of the solution phase also remained constant (Figure 3a→b). However, the **Hx**→**Hc** polymorph conversion proceeded when the film formation was prevented by macroscopic agitation (vide infra). We surmise that the **Hx** in the solution phase is most likely in an adsorption equilibrium with the adsorbed **Hx** on the cuvette surface, thus making them resistant to the polymorph conversion into **Hc** (Figure 3c).

To characterize the aforementioned film adhered to the cuvette wall, the solution phase was decanted from the cuvette (Figure 3b→c). This unveiled the adsorption of thin films faintly emitting in yellow throughout the inner walls of the cuvette (Figure 3c). The films displayed pronounced birefringence in polarized optical microscopic (POM) observation (Figure S6a), and AFM revealed the formation of anisotropically aligned **Hx** (Figure 3g). These observations compellingly suggest that the formation of **Hx** proceeds in an inhomogeneous manner, i.e., they are engendered through heterogeneous nucleation on a quartz surface, and furthermore, their nucleation might be catalyzed by themselves (secondary nucleation). This hypothesis was corroborated by variable temperature absorption measurements of **1** (c_t = 20 μM) during cooling with and without stirring (Figure S7). With stirring, spontaneous nucleation of **Hx** was evident from an abrupt onset of aggregation at 41 °C, which was accompanied by no film formation. Without stirring, in contrast, spontaneous nucleation evidently became more reluctant, as no such abrupt increase in the degree of aggregation was observed.

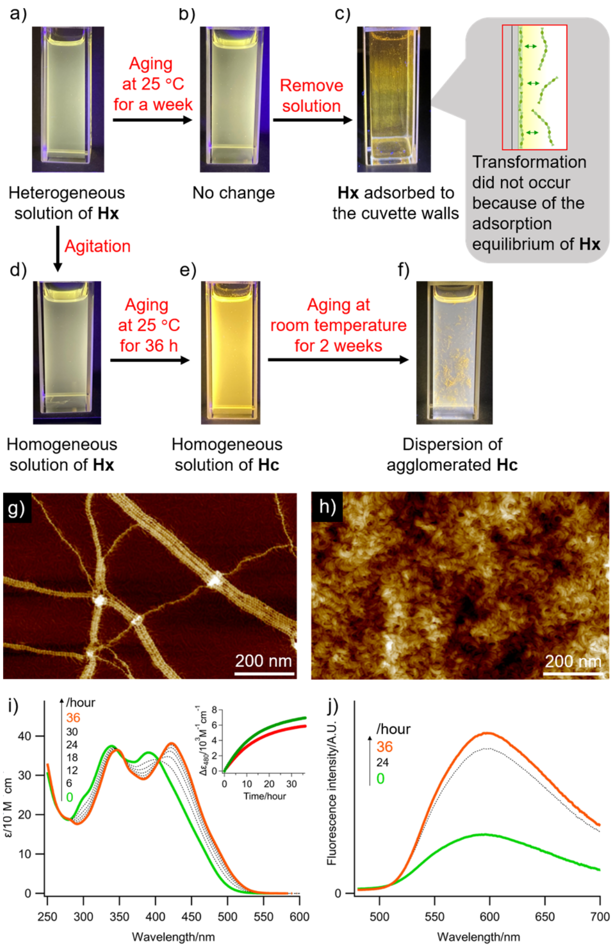

Figure 3. Photographs of (a,b,d,e) supramolecular polymer solutions, (c) films of **Hx**, and (f) precipitated **Hc** of **1** in 1.0-cm pathlength quartz cuvettes under 395 nm UV light. The starting sample (a) was prepared by cooling a c_t = 50 μM solution of **1** in CHCl$_3$/MCH = 70:30 mixture from 100 °C to 25 °C. For (c), a schematic illustration of the adsorption equilibrium between **Hx** in the solution phase and the adsorbed **Hx** on the cuvette surface is shown. (g) AFM image of the film adhered onto an inner wall of the quartz cuvette of the sample (c). The film was peeled from the cuvette by suspending using pure MCH. (h) AFM image of the precipitates of the sample (f). (i) Time-dependent changes of the absorption spectra during transition from the samples (d) to (e). Inset: time-dependent changes of ε at 480 nm when the sample (d) was aged as is (green dots, c_t= 50 μM) or aged after half-dilution (red dots, c_t= 25 μM). (j) Time-dependent change of the fluorescence spectra during transition from the samples (d) to (e). Excitation wavelength is 402 nm, an isosbestic point of the spectral change shown in (i).

The adhered **Hx** after cooling was readily dispersed by mechanical agitation (Figure 3a→d), and the resulting dispersion gradually transitioned to emit in yellow upon standing for 36 h at 25 °C (Figure 3d→e). Time-dependent absorption measurements demonstrated a significant shift of the absorption peak from 390 nm to 422 nm over 36 h (Figure 3i), denoting the **Hx**→**Hc** polymorph conversion. In fluorescence measurements, a 2–3 fold increase of emission intensity in visible region was recorded, with a slight redshift of emission maximum from 593 to 598 nm (Figure 3j). Upon further allowing the solution to stand for over a week at room temperature, fluffy precipitates were confirmed by naked-eye observation (Figure 3e→f). By AFM the precipitates were identified as highly entangled **Hc** (Figure 3h). In contrast to the **Hx** film, the **Hc** precipitates did not exhibit birefringence when observed by POM (Figure S6b), which reflects the isotropic agglomeration of highly folded **Hc**. The contrasting phase-separation behaviors of **Hx** and **Hc** underscore their distinct hierarchical organization properties as well as formation processes.

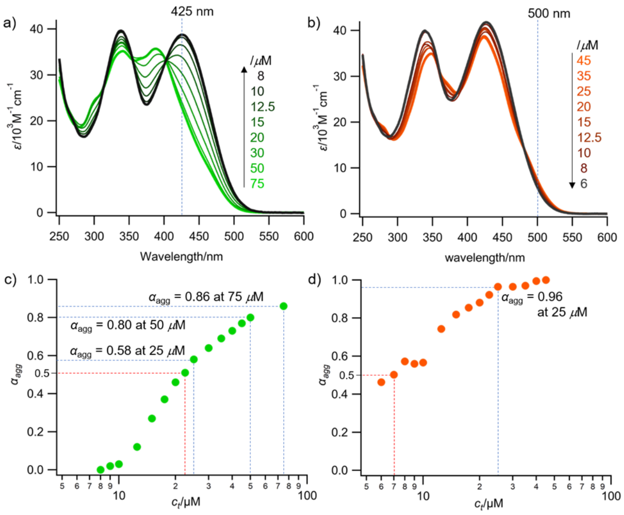

Figure 4. (a) Concentration-dependent absorption spectra of **1** showing the dissociation of **Hx** to monomers upon diluting a CHCl$_3$/MCH = 70:30 solution. **Hx** was obtained by cooling a solution of **1** (c_t= 50 μM) from 100 to 20 °C at a rate of 1 °C/min. This dilution experiment was performed at 20 °C (5 °C lower than 25 °C at which the conversion proceeds) for 150 min, during which transition from **Hx** to **Hc** was negligible (vide infra). (b) Concentration-dependent absorption spectra of **1** showing the dissociation of **Hc** to a mixture with monomer upon diluting another CHCl$_3$/MCH = 70:30 solution obtained by aging a **Hx** solution (c_t= 50 μM). (c,d) Plot of α_{agg} estimated from the absorption changes at 425 nm for (c) and at 500 nm for (d) as a function of c_t upon dilution.

Through the utilization of an extended conversion time achieved by the incorporation of MCH, we conducted concentration-dependent UV/vis measurements in a 70:30 CHCl$_3$/MCH mixture with the intention to compare the thermodynamic stability of **Hx** and **Hc**. In the case of **Hx**, we observed the growth of an absorption band at 425 nm upon dilution, indicating a progression towards monomerization (Figure 4a). This spectral change reached a plateau when the **Hx** solution was diluted approximately to c_t = 10 μM, implying a complete monomerization. Because it was not feasible to prepare a high concentration solution containing only **Hx** in this solution condition (the reason for this limitation will be elaborated in the subsequent section), the degree of aggregation (α_{agg}) of **Hx** was estimated by fitting the transition curve with the cooperative $K_{nucleation}/K_{elongation}$ model[62,63] (σ= 0.001 and $K_{elongation}$ =88000 M^{-1}, $K_{nucleation}$ = 88 M^{-1}, Figure S8). For the **Hc** solution, more moderate absorption spectral alterations were observed upon dilution (Figure 4b). This is partly because the absorption spectrum of **Hc** closely resembles to that of the monomer under this $CHCl_3$-rich condition, but also due to the fact that **Hc** did not dissociate completely into the monomeric state even upon dilution to c_t = 10 μM. A plot of α_{agg}, estimated from these absorption spectral changes versus c_t, revealed that the concentration at which half of the assembly was monomerized (c_t at $\alpha_{agg} = 0.5$) was found at c_t = 22.5 μM for **Hx** whereas c_t = 7 μM for **Hc** (Figure 4c,d). This provides a clear illustration of the superior thermodynamic stability of **Hc** over **Hx**.

Notably, when the **Hx**→**Hc** conversion experiment in the 70:30 $CHCl_3$/MCH mixture was conducted after a half dilution of the initial **Hx** solution (c_t = 50 to 25 μM), no substantial difference in their kinetics was observed and the transition proceeded exponentially, aligning with first-order reaction kinetics with nearly identical kinetic constants (k = 0.073 and 0.069 h^{-1} at c_t = 50 and 25μM, respectively, inset in Figure 3i). Although this dilution decreases the degree of aggregation (α_{agg}) in **Hx** from 0.80 to 0.58 (see Figure 4c), the resulting free monomers do not form **Hc** even though α_{agg} in **Hc** at c_t = 25μM is 0.96 (see Figure 4d). This concentration-independent kinetics accordingly suggests a direct conversion of **Hx** to **Hc** without monomer dissociation and reassembly.[46,65,66]

Time-dependent AFM measurements during the **Hx**→**Hc** polymorph conversion (Figures 3d→3e) distinctly verified that the direct structural transition from the twisted to the helically folded morphologies of the supramolecular polymer chains. Figure 5 showcases AFM images captured after 7-h duration from the maturing **Hx** solution at 25 °C. All of the images, inclusive of those presented in Figures S9 and S10, unambiguously delineate the connection of the two supramolecular polymer polymorphs, forming chimeric block structures. This was substantiated by AFM height analysis at the junction point, which demonstrated abrupt alterations in fiber heights (Figure 5a, inset). As far as could be ascertained, all the chimeric structures encompass either

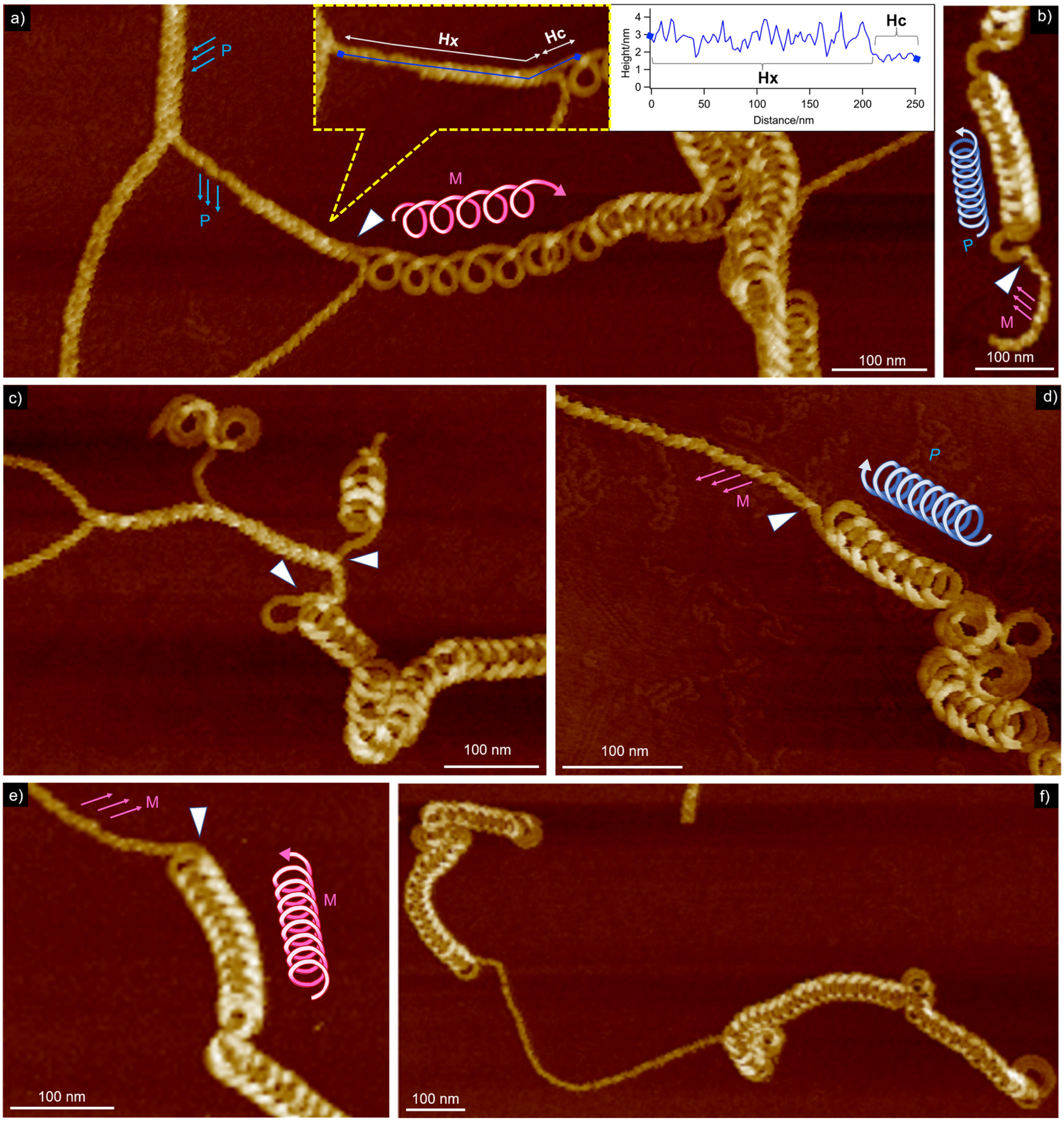

Figure 5. (a–e) AFM images of block fibers observed during the **Hx**→**Hc** polymorph transition. White arrows indicate where the transition from **Hx** begins. Inset in (a) is height analysis for a junction point. (f) An example of **Hc**-**Hx**-**Hc** triblock structure. The pink and blue linear (for **Hx**) and helical (for **Hc**) arrows indicate the M- and P-helices, respectively.

an **Hc**–**Hx**–**Hc** triblock (Figure 5f, S10a) or **Hx**–**Hc** diblock structures. The absence of **Hx**–**Hc**–**Hx** triblock structures or multiblock structures, wherein a **Hc** block is sandwiched between **Hx** blocks, suggest that the structural conversion is solely initiated from the **Hx** termini, at which one rosette facet is solvated, thereby facilitating the rearrangement of molecular conformations. This is further corroborated by the acceleration of the overall polymorph conversion kinetics for a mechanically fragmented **Hx** solution. The original **Hx** fibers, present within the Figure 3d solution, exceeded lengths of 25 μm (Figure S11), and exhibited no polymorph conversion according to AFM (Figure S12a→c) and UV/vis (Figure S12e) measurements at 20 °C (5 °C lower than 25 °C at which the conversion proceeds). Upon the ultrasonication (40 kHz) of the **Hx** solution for 1 min, the majority of **Hx** fibers were fragmented to lengths of less than 500 nm (Figure S12b). Upon aging the fragmented sample for 1 day at 20 °C, the conversion of 25 mol% of total molecules from **Hx** to **Hc** was observed according to AFM (Figure S12b→d) and UV/vis (Figure S12f) measurements.

In summation, it is apparent that **Hc** is not directly accessible from the molecularly dissolved state, and the kinetic formation of **Hx** invariably precedes its formation. Owing to a large supramolecular π-conjugated system, $\mathbf{1}_6$ rosettes kinetically aggregate without satisfying the optimal stacking structure required to induce curvature.

Influence of Residual Assemblies. In the preceding section, the initial pure **Hx** solution was prepared by dissolving the film of **Hc** and toroid in a 70:30 $CHCl_3$/MCH mixture by heating to 100 °C (hereafter defined as T_{max}), and subsequently polymerizing the resulting monomers through cooling. If the solution at T_{max} consists solely of monomeric species, the nucleation process toward **Hx** emerges as the exclusive feasible pathway. However, should a miniscule amount of **Hc** with polymer termini survive at T_{max}, two potential assembly pathways would be presented for the monomers; the nucleation of **Hx** and the elongation of the existing **Hc**-seed. In this section, we illustrate an example wherein the residual assemblies could lead to intricate outcomes on products contingent on the polymerization conditions, employing the current polymorphic system.[67–70]

The first example of a condition wherein **Hc** survives at elevated temperatures is when the solvent system encompasses a significant quantity of MCH, which promotes polymerization. Upon dissolving the film of **Hc** and toroids (c_t = 50 μM) in $CHCl_3$/MCH = 50:50 and 30:70 mixtures through ultrasonication and heating to T_{max} of 100 °C, homogeneous solutions were achieved, analogous to the case of the $CHCl_3$/MCH = 70:30 mixture (Figure 6a). On cooling these solutions to 20 °C at a rate of 1 °C/min, both **Hx** and **Hc** were observable by AFM (Figure 6c,d). The higher the MCH fraction, the fewer **Hx** and the more **Hc** were observed. Given that low polar solvents render supramolecular polymerization more irreversible, increasing MCH should yield kinetic products (**Hx** in this study).[71] The contrary trend observed thus serves as the first indication of the influence of **Hc** remaining at T_{max}. Indeed, **Hc** and toroids were observable when spin-coating the $CHCl_3$/MCH = 50:50 solution at 100 °C, but not even trace aggregates were discernible when spin-coating a $CHCl_3$/MCH = 70:30 solution at 60°C (Figure S13).

Another condition that influences the quantity of **Hc** surviving at T_{max} is total concentration of monomers (c_t). The effect of c_t on the reversibility of supramolecular polymerization would postulate that reducing c_t (thus augmenting the degree of reversibility) would yield more of the thermodynamic product (**Hc**). As demonstrated in Figure 6e–g, however, an increase in the yield of **Hx** was observed when c_t was decreased from 200 to 20 μM for solutions in $CHCl_3$/MCH = 50:50 at T_{max} = 100 °C. The observation that the thermodynamic product, **Hc**, is obtained at higher c_t suggests that these outcomes cannot be elucidated solely by the kinetic and thermodynamic considerations of supramolecular polymerization.

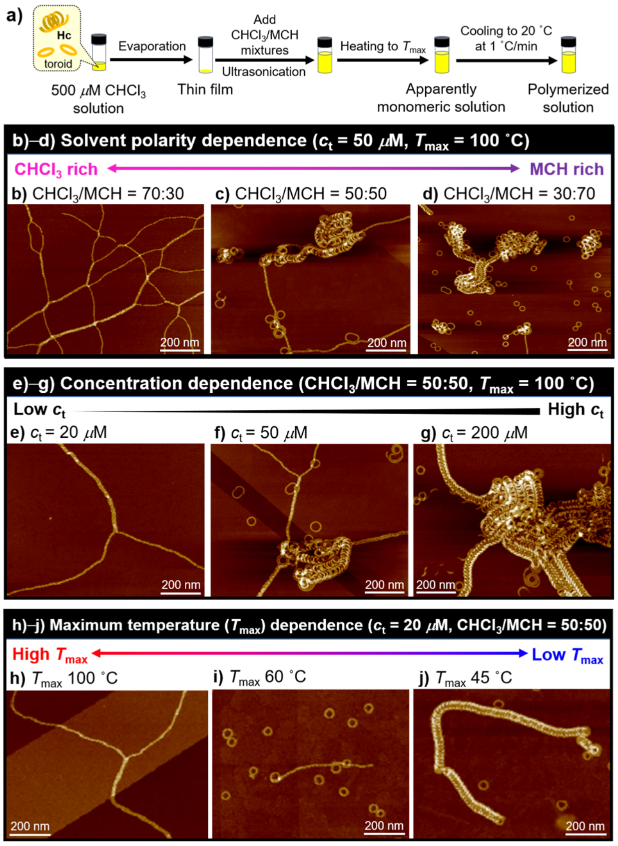

Figure 6. (a) Schematic illustration for the sample preparation method of supramolecular polymers of **1** in $CHCl_3$/MCH mixtures, starting from a $CHCl_3$ solution (c_t = 500 μM). (b–d) AFM images of assemblies upon changing ratio of $CHCl_3$ and MCH (c_t = 50 μM; T_{max} = 100 °C). (e–g) AFM images of assemblies upon changing c_t for $CHCl_3$/MCH = 50:50 solutions (T_{max} = 100 °C). (h–j) AFM images of assemblies upon changing T_{max} for $CHCl_3$/MCH = 50:50 solutions (c_t = 20 μM). All AFM images shown in (b–j) correspond to absorption spectra shown in Figure S14(b–j).

To procure a more compelling result that manifests the influence of the surviving **Hc** at T_{max} on the pathway complexity to **Hx** and **Hc**, we employed a lower T_{max} to vary the quantity of surviving **Hc** for the $CHCl_3$/MCH =50:50 solution at c_t = 20 μM, from which **Hx** was exclusively obtained when T_{max} = 100 °C (Figure 6h). By reducing T_{max} to 60 °C, at which point **Hc** is predominantly dissociated into monomers while the toroids remain intact (Figure S15), we obtained a mixture of **Hx** and toroids (Figure 6i). With a considerably lower T_{max}, for instance 45 °C, at which approximately 53% of **Hc** was dissociated to yield monomers while the toroids survived (Figure S15), we obtained **Hc** and toroids, with **Hx** scarcely detected (Figure 6j).

The dependencies of the distribution ratio of monomers to **Hx** and **Hc**, contingent on the solvent composition, total concentration of monomers (c_t) and maximum temperature (T_{max}), can be organized into three categories—conditions A through C—as depicted in Figure 7a. Our experimental design, illustrated in Figure 6a, entailed the preparation of a film from the $CHCl_3$ solution (with c_t = 500 μM), containing **Hc** and toroids. This was subsequently dissolved in $CHCl_3$/MCH mixtures via heating to T_{max}. Consequently, these solutions, which ostensibly appear monomeric, may contain varying amounts of residual **Hc** depending on the prevailing conditions.

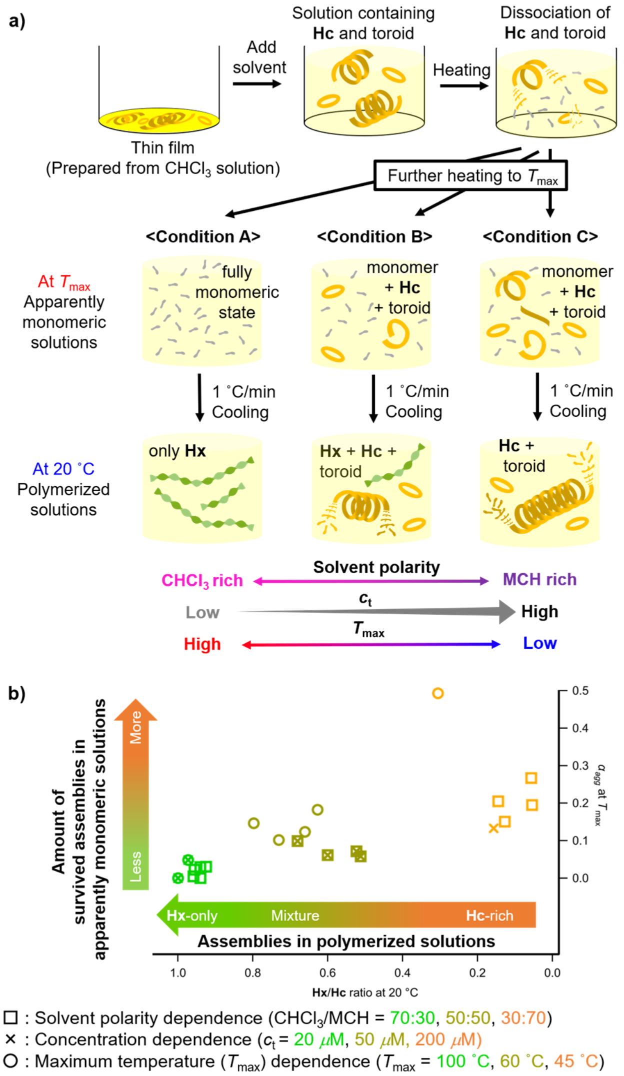

Figure 7. (a) Schematic illustration to show how **Hc** and toroids in the film state cause complex outcome on the products through heating (to T_{max}) and cooling procedures under different conditions A–C. (b) A scatter plot of α_{agg} at T_{max}, an indicator of the amount of survived assemblies at T_{max}, and the resulting **Hx**/**Hc** ratio at 20 °C after cooling at a rate of 1 °C/min for solutions of **1** under various conditions. The shapes of the markers represent the variable parameters: squares represent the results upon changing $CHCl_3$/MCH ratio (corresponding to Figures 6b-d), crosses represent the results upon changing c_t of **1** (corresponding to Figures 6e-g), and circles represent the results upon changing T_{max} (corresponding to Figures 6h-j). Colors of arrows and marks are qualitative indicators for the survived **Hc** (richer in orange, poorer in green) and the resulting assemblies (orange and green represents richer in **Hc** and **Hx**, respectively).

Lowering c_t, increasing chloroform content, or applying higher T_{max} engenders a fully monomeric state at T_{max}. From such a state, only **Hx** could be obtained (Figure 6b,e,h and condition A in Figure 7a). Conversely, increasing c_t, diminishing chloroform content, or implementing lower T_{max} could increase the amount of residual **Hc** at T_{max}. Under these conditions, the elongation of **Hc** from the surviving species occurs upon cooling, resulting in **Hc** becoming the dominant product (Figure 6d,g,j and condition C in Figure 7a). When the amounts of the monomer and the surviving **Hc** are antagonistic at T_{max}, the nucleation of monomers leading to **Hx** and elongation from the surviving **Hc** compete. Consequently, all types of assemblies (**Hx**, **Hc** and toroid) could be obtained through cooling (Figure 6c,f,i and condition B in Figure 7a). Based on this understanding, we estimated the degree of aggregated molecules (α_{agg}) at T_{max} and the resulting **Hx**/**Hc** ratio after cooling through absorption measurements under various conditions (Figure S14, for details, see the Supporting Information). As Figure 7b demonstrates, there is a clear correlation between α_{agg} at T_{max} and the **Hx**/**Hc** ratio when the solvent composition, c_t and T_{max} are varied.

It is of further note that the **Hc** products obtained under condition C in Figure 7a did not precipitate, contrasting with the **Hc** products obtained via the **Hx**→**Hc** polymorph conversion under condition A. At the identical concentration of c_t = 50 μM, the former **Hc**, elongated from the surviving **Hc**, have lengths of approximately 3 μm (Figure 6d), while the latter **Hc**, formed via **Hx**, reach 10 μm before precipitation (Figure S16). Moreover, the former was contaminated with toroids (Figure 6d), whereas the latter was devoid of such contamination (Figure S16).

These findings underscore the significance of supramolecular polymerization protocols related to the monomeric state wield substantial impact on the properties of the final supramolecular products. These results exemplify the importance of meticulously assessing the status of "seemingly monomeric" solutions of compounds exhibiting supramolecular polymorphs, depending on concentration, solvent, and initiation temperature. It is pertinent to acknowledge that the distribution of self-assembled products may not solely be determined by the pathway complexity imposed by kinetic barriers toward distinct supramolecular polymorphic states.

Photophysical and Structural Properties. Following the successful establishment of protocols for acquiring pure **Hx** and **Hc**, we directed our investigation towards the photophysical properties exhibited by these supramolecular polymer polymorphs. To juxtapose their absorption and fluorescence spectra under identical conditions, we prepared pure **Hx** and **Hc** solutions in 10:90 $CHCl_3$/MCH mixture at c_t = 10 μM by diluting appropriate solutions with MCH. As shown in Figure 8a, distinct absorption and fluorescence signatures were recorded for **Hx** and **Hc**. When compared to the absorption spectrum of the monomeric state, acquired at 100 °C post dilution of these solutions to c_t = 1.5 μM, the absorption spectrum of **Hx** exhibited a hypsochromic and hypochromic shift. Furthermore, the emission intensity of **Hx** proven to be inferior to that of the monomeric state, with its quantum yield (Φ_f) measured as 0.02 in the solution state. Conversely, the absorption spectrum of **Hc** displayed a bathochromic shift relative to that of the monomer, accompanying by a newfound absorption shoulder at 480 nm. In addition to this observation, **Hc** demonstrated enhanced fluorescence, registering Φ_f of 0.12. These highly contrasting aggregation-induced changes in the photophysical properties signify that the rosettes within **Hx** and **Hc** conform a face-to-face (H-type) and offset (J-type) stacking arrangements,[7–10] respectively. Moreover FT-IR measurements corroborated that **Hx** and **Hc** possess the identical hydrogen-bonded pattern of barbituric acid moieties (Figure S17). Thus, it is postulated that the supramolecular polymer polymorphism is solely attributable to the unique stacking arrangements of the rosettes.

Since the starkly disparate photophysical properties of **Hx** and **Hc** are indicative of pronounced differences in their structures, a comparison of the structural properties of **Hx** and **Hc** was conducted in solution by means of SAXS. Owing to known issues pertaining to X-ray absorption by chloroform, the solvent mixtures utilized for the preparation of **Hx** and **Hc** were substituted with pure MCH (for sample preparation, see the Supporting Information). AFM analysis revealed that this change in solvent had no discernible effect on the morphologies of the assemblies (Figure S18). The SAXS profile of **Hx** does not exhibit the nonperiodic oscillatory feature that is characteristic of our curved supramolecular polymers[72,73] and is consistent with the linearly extended fibrous morphology (Figure 8b, green curve). The scattering data of **Hx** fits well to a model representing a cylinder with an elliptical cross-section (Figure 8c).[74] Details of all SAXS data fitting are given in the Supporting Information.[75] The ellipsoidal cross-section of **Hx** corroborates a tilted stacking arrangement of $\mathbf{1}_6$ rosettes within the assembly. In solution, the longer diameter of ellipsoid was estimated to measure approximately 9 ± 1 nm (Table 1). Given that the SAXS signal is predominantly derived from the aromatic and barbituric acid sections of the $\mathbf{1}_6$ rosettes, and not the outer alkyl chains, it is plausible to infer that the longer diameter of **Hx** is calculated slightly smaller than the dimensions of the entire rosette, as estimated by molecular modelling (around 10 nm; Figure 1b). Conversely, the SAXS profile of **Hc** displays a distinct scattering profile marked by nonperiodic oscillatory feature at Q = 0.1–1 nm^{-1}, which arise from the intrinsic curvature of supramolecular polymer chains (Figure 8b, orange curve).[73] The profile fitted well to a model representing a hollow cylinder,[73] finding 35 ± 2 nm for the center-to-center diameter (Table 1, Figure 8c).

Structural details, unattainable through the utilization of SAXS, were acquired by means of both AFM and transmission electron microscopy (TEM) imaging. These imaging were performed on samples that had been transferred to appropriate substrates using a solution processing. While acknowledging the potential for deformation of these delicate structures due to the solution process, the conjunctive application of AFM and TEM nonetheless contributes invaluable supportive data to the SAXS findings (Table 1).

Regarding the AFM images of **Hx**, an alternation of bright and dark areas along the fiber axis implies the existence of a twisted helical structure (Figure 8d). Upon orthogonal height analysis of the fiber axis, these alternating regions present

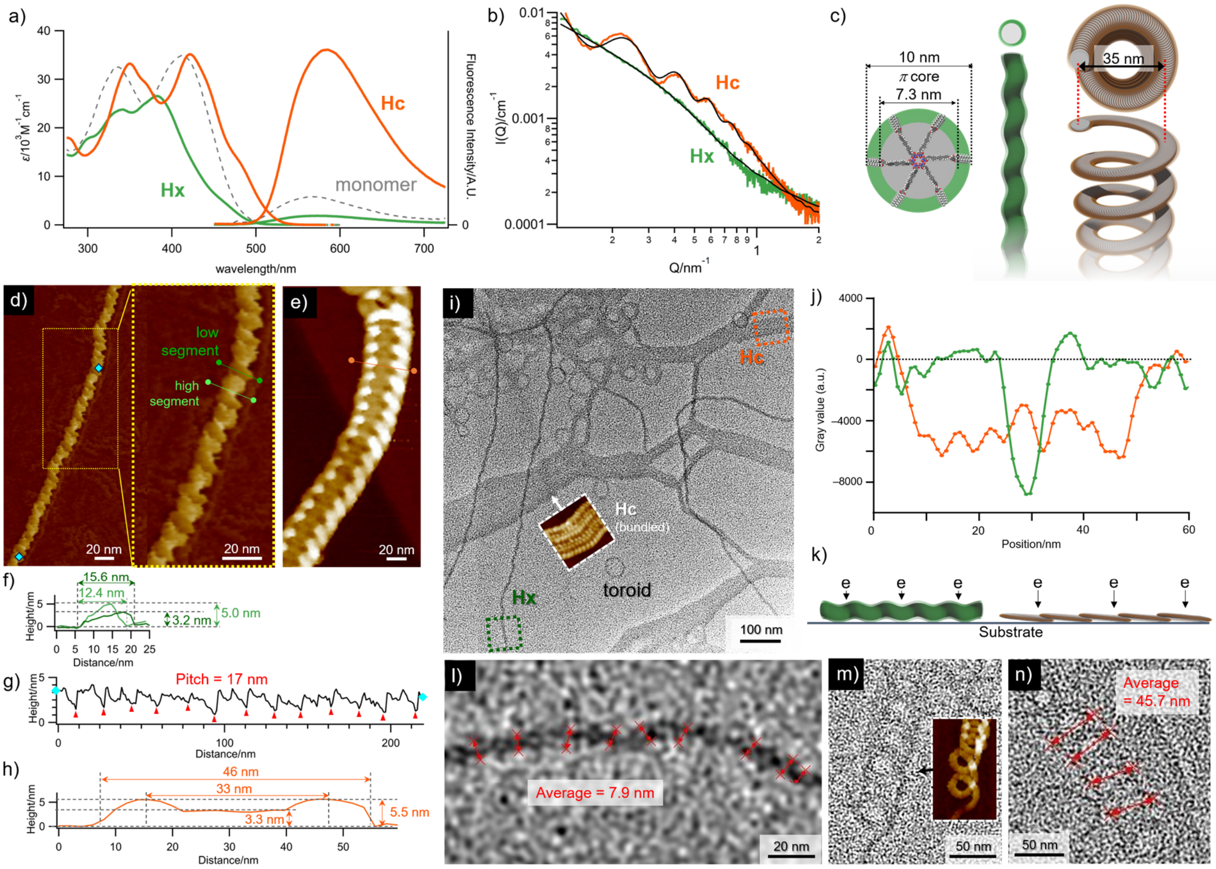

Figure 8. (a) Absorption and fluorescence spectra (λ_{ex} = 420 nm) of **Hx** (green) and **Hc** (orange) at 20 °C, and monomeric **1** (gray) at 100 °C in $CHCl_3$/MCH = 10:90. c_t = 10 μM for **Hx** and **Hc**, and 1.5 μM for the monomer. For **Hx**, c_t = 50 μM solution in $CHCl_3$/MCH = 70:30 was cooled from 100 to 20 °C at the rate of 1 °C/min. For **Hc**, c_t = 20 μM solution in $CHCl_3$/MCH = 20:80 was cooled from 100 to 20 °C at the rate of 1 °C/min. Both assembly solutions were then diluted with MCH to afford c_t = 10 μM solutions in $CHCl_3$/MCH = 10:90. (b) SAXS profiles of **Hx** (green) and **Hc** (orange). c_t = 100 μM in MCH. The black lines are fits to the data using a model representing a cylinder with an elliptical cross-section for **Hx**, a model representing a hollow cylinder for **Hc**, respectively. (c) Cartoon image of **Hx** and **Hc** reproduced by stacking a disc with the diameter of 10 nm and the thickness of 0.2 nm assuming $\mathbf{1}_6$ rosette. The center-to-center diameter of **Hc** are consistent with those from SAXS. (d) Magnified AFM image of **Hx**. (e) Magnified AFM image of **Hc**. (f) The height analysis orthogonal to the fiber axis of **Hx** shown in panel (d) between green dots and light-green dots. (g) The height analysis parallel to the fiber axis of **Hx** shown in panel (d) between sky-blue dots. (h) The height analysis orthogonal to the helicoid axis of **Hc** shown in panel (e) between orange dots. (i) Transmission electron microscope (TEM) image of **Hx**, **Hc** and toroids of **1**. In case the helical structure of the **Hc** is tightly packed, it cannot be distinguished and appears like a band in the TEM image, as indicated with the inset AFM image. (j) Intensity profile of the selected areas in the TEM image for **Hx** (green square in i) and **Hc** (orange square in i). (k) Cartoon image of **Hx** and **Hc** on the substrate. (l) Magnified TEM image of **Hx** used to estimate the width. (m,n) Magnified TEM images of **Hc** used to estimate the outer diameter.

with heights of approximately 5.0 nm and 3.2 nm, respectively (Figure 8f). Height analysis along the fiber axis of **Hx** revealed the presence of periodic helix pitch of approximately 17 nm (Figure 8g). Furthermore, the distinctive features of both left-handed (*M*) and right-handed (*P*) helicities were prominently discernible (Figure 5, S19a,b). Such an ellipsoidal structure with a periodic pitch might result from the sequential stacking of slightly tilted rosettes following a helical trajectory.

Table 1. Structural parameter of **Hx** and **Hc** derived from SAXS, AFM and TEM measurement.

	SAXS	AFM	TEM
Hx			
height of main chain		5.0 nm[b] 3.2 nm[c]	
width of main chain	9 ± 1 nm[a]	12.4 nm[b] 15.6 nm[c]	7.9 nm
helical pitch		17 nm	
Hc			
height of main chain		3.3 nm	
width of main chain		11.5 nm	
fiber center-to-fiber center diameter	35 ± 2 nm	33.0 nm	
outer diameter		46.0 nm	45.7 nm

[a] longer diameter of ellipsoid. [b] higher segment, [c] lower segment in Figure 8(d).

Conversely, the AFM height analysis orthogonal to the helicoid axis of **Hc** (Figure 8e) showed a height profile of alternating high (5.5 nm) and low (3.3 nm) elevations, corresponding to a flattened helicoid (Figure 8h). This flattening process appears to take place without altering the curvature, as evidenced by the fiber center-to-fiber center diameter of **Hc**, as visualized by AFM (33 nm), being in substantial alignment with the diameter estimated from the SAXS analysis (35 nm). Thus, the supramolecular polymer main chain of **Hc** is believed to consist of flat tapelike fibers with thickness of 3 nm, suggesting a pronounced tilting of rosettes. The helical handedness of **Hc**, however, is not invariably evident in the AFM images, but to the extent determinable, the formation of both and *P*- and *M*-helicoids has been observed (Figure 5, S19c). It is of importance to note that the helical handedness is not consistently maintained during the **Hx**→**Hc** polymorph transition. Both *M*-helix to *M*-helicoid (Figure 5e) and *M*-helix to *P*-helicoid (Figure 5d) conversion have been observed.

TEM imaging of **Hx** and **Hc**, coupled with image contrast analysis, contributes complementary structural information to that obtained via AFM. The image contrast of **Hx** is higher than that of **Hc** (Figure 8i,j), proposing a greater density of molecules per unit area within **Hx** on the supporting film in comparison to **Hc**. This may reflect the more vertical orientation of the π-plane of the **1**$_6$ rosettes within the **Hx** fiber relative to those within the **Hc** fiber, potentially due to the flattening of the helicoidal structure of **Hc** (Figure 8k). The visible width of the **Hx** fiber within the TEM images is approximately 7.9 nm (Figure 8l), which is shorter than that measured by AFM (12.4 nm), yet aligns more closely with the dimensions obtained through SAXS analysis (approximately 9 nm). This difference implies that the image contrast of the alkyl chains within **Hx** is relatively weak and is obscured by the background signal arising from the support film.[76] Consequently, only the aromatic and barbituric acid sections appear discernible in the TEM image. In contrast, the **Hc** fiber, which presents the π-plane of the **1**$_6$ rosettes oriented nearly parallel to the substrate, does not exhibit significant image contrast between the aromatic and alkyl chain domains. Thus, the outer diameter of **Hc** as analyzed by TEM (45.7 nm) aligns almost precisely with that determined by AFM (46 nm, Figure 8m,n).

Modeling Studies. Based on the well-characterized helical morphologies and dimensions of **Hx** and **Hc** as discerned through SAXS, AFM and TEM, coupled with their distinct spectroscopic signatures, we conducted molecular modeling simulations to garner a deeper understanding of the connection between local stacking of **1**$_6$ rosettes and the resultant helical morphologies. Using experimentally derived values of the helical pitch (*P*) and the helical radius (*R*) for both assemblies, we undertook an investigation into the most stable stacking structure of **1**$_6$ rosettes that could replicate the *R* and *P* values. A helical morphology is chiefly dictated by the number of the rosettes per pitch (*Nc*) and the tilt angle of the rosette to the xy-plane (*Cx,* see Figure 9a). The parameter *Cx* also affects the degree of flattening of the main chain. The rotation angle of the rosette per stacking (*Cz*) similarly demonstrates a substantial role in the stability of the stacking structure, working in conjunction with *Nc* and *Cz*.

We constructed 144026 initial structures based on all possible combinations of *Nc*, *Cx* and *Cz* so that *R* and *P* are consistent with the experimental data. Subsequently, energy minimization and potential energy calculations were performed for trimeric rosette stacks extracted from all the initial structures. Given the periodic structures of **Hx** and **Hc**, it is unnecessary to calculate the potential energy for the entire rosette stacks. The potential energies post-minimization were computed, and ordered in decreasing fashion, and the parameter sets yielding the lowest potential energy were used to reconstruct **Hx** and **Hc** as shown in Figure 9b and 9e (for details, see Supporting Information). Table 2 outlines the parameters associated with the lowest potential energy. From the order list of the potential energies (Supporting Information), the number of parameter sets exhibiting an energy difference of less than 50 kcal/mol from the most stable structure was 88 for **Hx**, with an average *Nc* of 52 ± 5, whereas 1430 for **Hc**, with *Nc* ranging from 65 to 140. These results suggest that **Hx** has a more rigid structure, while **Hc** possesses a flexible structure with a distribution in the number of **1**$_6$ rosettes per pitch.

Table 2. The parameters of the most stable structure with the lowest potential energy for **Hx** and **Hc**.

	Hx	**Hc**
helical Pitch (*P*)/nm	17	17
helical radius (*R*) /nm	1.03	17.5
number of rosettes per pitch (*Nc*)	52	112
tilt angle of rosette (*Cx*) /degree	2	12
rotation angle of rosette (*Cz*) /degree	0	9
inter rosette distance (d_i) /nm	0.33	0.35
translational displacement of rosette (d_t) /nm	0.11	0.93
potential energy / kcal/mol	-3980	-3807

Figure 9b and 9e depict all-atoms models of **Hx** and **Hc** structures, respectively, obtained through energy minimization of all rosettes in the initial structure constructed using the optimized parameters listed in Table 2. The all-atom structures replicate well the alternating concave and convex structures of **Hx**, as well as the flattened loops of **Hc** as visualized by AFM. On the other hand, the models without alkyl chains represent the appearance delineated by the π-conjugated units, which consistent with what we observed through SAXS and TEM experiments (Figure 9c and 9f). Furthermore, the distinct helical trajectories of **1**$_6$ rosette in these structures can be represented by displaying only barbituric acid cores (Figure 9d and 9g).

In the actual self-assembly process, the helical trajectories delineated by the rosette can be defined via stacking parameters between two adjacent rosettes including the translational displacement (d_t) and the cofacial distance (d_i)

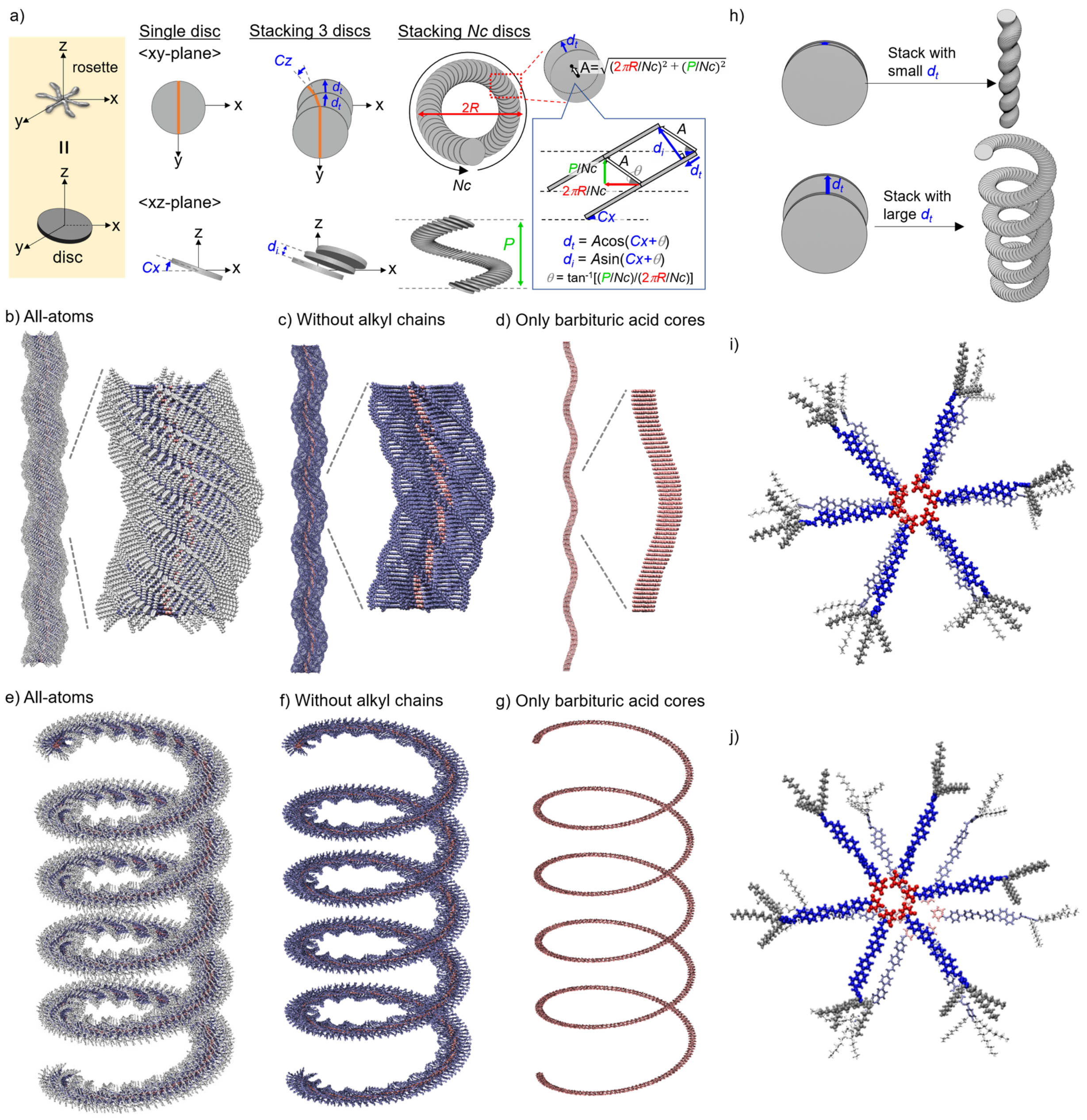

Figure 9. (a) Schematic diagram depicting parameters determining the structures of **Hc** and **Hc**, helical pitch (P), helical radius (R), number of rosettes per pitch (Nc), tilt angle of rosette (Cx), rotation angle of rosette (Cz), translational displacement of rosette (d_t), and inter-rosette distance (d_i). The rosettes are represented as discs for simplicity. (b–d, e–g) Molecular models of **Hx** (b–d) and **Hc** (e–g), built from the structural parameters listed in Table 2 and subsequent energy minimization of all rosettes within the lattice. (b,e) all-atom representations, (c,f) representations without alkyl chains, and (d,g) representation with only barbituric acid cores. (h) Schematic representation showing that small and large d_t result in **Hx** and **Hc**, respectively. (i,j) Visualization of stacking arrangements of two rosettes within (b) and (e), respectively.

as shown in Figure 9a, in addition to Cx and Cz. The d_t and d_i can be calculated using P, R, Nc and Cx as follows (see Figure 9a);

$$d_t = \sqrt{(2\pi R/Nc)^2 + (P/Nc)^2}\,\cos\{Cx + tan^{-1}[(P/Nc)/(2\pi R/Nc)]\}$$

$$d_i = \sqrt{(2\pi R/Nc)^2 + (P/Nc)^2}\,\sin\{Cx + tan^{-1}[(P/Nc)/(2\pi R/Nc)]\}$$

The calculated d_i of **Hx** (0.33 nm) and **Hc** (0.35 nm) are comparable to those observed for columnar mesophases of discotic (supra)molecules, and is not the major factor that engenders polymorphs. In contrast, d_t exerts the greatest influence on determining the final assembly structure. A small d_t engenders an **Hx**-like structure, while a large d_t gives rise to an **Hc**-like structure (Figure 9h). For the simulated **Hx** and **Hc** structures, d_t values were calculated to be 0.11 and 0.93 nm, respectively. The smaller d_t in **Hx** enables all six π-conjugated units in a rosette stacking in face-to-face arrangement, which is consistent with the spectroscopic properties (Figures 9i). The larger d_t in **Hc**, on the other hand, does not allow homogeneous stacking for six π-conjugated units and only partially overlap is allowed (Figure 9j). This may explain why the absorption spectrum of **Hc** does not significantly differ from that of the monomer. These findings highlight that the difference in d_t is the major determinant for the two polymorphs, and the **Hx**→**Hc** transition is driven by the H-to-J type dislocation of rosette stacks.

DISCUSSION

The photophysical data coupled with molecular modeling simulations unequivocally illustrate that the two polymorphs, **Hx** and **Hc**, can be differentiated predicated upon the stacking geometry of rosettes. The conversion from **Hx** to **Hc** occurs under appropriate conditions, and the results of the concentration-dependent absorption measurements furnish definitive proof that **Hc** possesses superior thermodynamically stability. The thermodynamic instability of **Hx** may be ascribed to the dipole repulsion between the face-to-face stacked $\mathbf{1}_6$ rosettes. A comparable polymorphism is not evident for compound **2** possessing a shorter π-conjugated system and a dipole moment of 5.9 D. Consequently, $\mathbf{1}_6$ rosettes exhibit enhanced cohesion attributable to the expansion of the π-conjugated system, which initially favors H-type aggregation by overcoming dipole repulsion between π-conjugated units with dipole moment of 7.5 D. The experimentally observed thermodynamic stability of **Hc**, despite the offset stack of rosettes, is largely dependent upon interloop interactions, which is a unique feature of the helicoidal structure.[51] It should be noted that the geometry optimization suggests that **Hx** is slightly thermodynamically stable. This may reflect the absence of interloop interaction in the present modeling study. As part of a collaborative effort, molecular dynamic simulations of more elongated **Hc** inclusive of solvent molecules are currently under way.

The alteration in the rosette stacking geometry that arises during the **Hx**→**Hc** polymorph conversion proliferates along the main chain, resembling a crystal transition, as captured in time-dependent AFM images. At the macroscopic level, the transition manifests first-order kinetics, suggesting progression by a mechanism akin to nucleation. Following the initiation of the transition, several hours elapse before propagation occurs through the **Hx** chain across several tens of micrometers. Consequently, both fully folded **Hc** with completed conversion and remaining **Hx** devoid of any conversion can coexist (Figure S16). It is important to recognize that the helicity of **Hx** is not invariably preserved during its transition to **Hc**, as illustrated in Figure 5. Specifically, the kinetic H-aggregated state with a large rosette overlap initially transitions to an assembly state with a reduced rosette overlap (H-to-J type dislocation). At this juncture, the helicity of **Hx** has already been lost, but the intrinsic curvature has yet emerge because the rotational direction of rosette stacking remains unfixed, as demonstrated in Figure 5a-d. Further reorganization of the rosette stacking towards a thermodynamically stable configuration gives rise to the intrinsic curvature. Upon the formation of a uniform intrinsic curvature to generate a loop, interloop interactions serve to stabilize the resultant helicoidal structure, functioning as a template to expedite the collapse of **Hx** and its folding into **Hc**.

CONCLUSION

In this study, we have presented evidence of a supramolecular polymer polymorphism, in which large discotic non-covalent macrocycles (rosettes) stack in a one-dimensional fashion. One such polymorph, a helically twisted fiber referred to as **Hx**, is derived from the supramolecular polymerization of the monomer. In contrast, a helicoidal fiber (an intrinsically curved structure), denoted as **Hc**, cannot be derived directly from the monomer. Rather, it is produced through a higher-order folding process of **Hx**, not by monomer dissociation and re-assembly. When a monomer-rich solution retains residual fragments of **Hc**, the elongation of **Hc** demonstrates superiority over the nucleation of **Hx**. These two supramolecular polymer polymorphs are spectroscopically distinguishable, each presenting unique absorption and fluorescence signatures attributed to divergent rosette stacking with smaller (H-type) and larger (J-type) translational offset. Our modelling simulation has indicated that continuous rosette stacking with varying degrees of translational offset could engender the formation of the twisted and helicoidal supramolecular polymers. Intriguingly, these two supramolecular polymer polymorphs exhibit macroscopically observable higher-order organization (phase separation) properties during time-dependent spontaneous folding. The two polymorphs demonstrate bistability in low-polarity solvent mixtures; however, in high-polarity solvent mixture, **Hx** gradually fold into **Hc** from their termini. AFM clearly reveals the linkage between these two distinctly different helical structures, demonstrating unequivocally that the transition from **Hx** to **Hc** is incited by a H→J type dislocation of the stacked rosettes.

We would like to underscore the significance of our findings in this research, particularly the enlargement of the π-conjugated system and the amplified π-π interaction between the monomers. These enhancements facilitated the creation of two forms of helical one-dimensional supramolecular polymers with meso-to-microscopic lengths. This amplified interaction is robust enough to enable the formation of mesoscopic assemblies in chloroform, a solvent typically employed for achieving a molecularly dissolved state in the majority of π-system based supramolecular compounds. This insight has led us to a newfound cautionary point concerning the influence of residual assemblies on supramolecular polymorphism. While the synthesis of self-assembling monomers, characterized by a strong propensity for aggregation, is synthetically challenging,[77,78] we were able to overcome these hurdles in this system by extending the pseudo π-system through hydrogen bonding. Our research continues to explore the use of even larger π-conjugated monomers, an approach aimed at broadening the range of suitable solvents for these processes.[2]

ASSOCIATED CONTENT

Supporting Information

The Supporting Information is available free of charge on the ACS Publications website.

Experimental details, synthetic procedures, compound characterization data, AFM images, spectroscopic data, SAXS analyses and details of structural simulation (PDF). A Microsoft Excel spreadsheet of the potential energy with various structural parameters for **Hc** and **Hx** assemblies (potential energy.xlsx).

AUTHOR INFORMATION

Corresponding Authors

Shiki Yagai – Institute for Advanced Academic Research (IAAR), Chiba University, Chiba 263-8522, Japan; Department of Applied Chemistry and Biotechnology, Graduate School of Engineering, Chiba University, Chiba 263-8522, Japan; orcid.org/0000-0002-4786-8603; Email: yagai@faculty.chiba-u.jp

Takahiro Ohkubo – Division of Advanced Science and Engineering, Graduate School of Science and Engineering, Chiba University, Chiba 263-8522, Japan; orcid.org/0000-0001-8187-1470; Email: ohkubo.takahiro@faculty.chiba-u.jp

Martin J. Hollamby – Department of Chemistry, School of Chemical and Physical Sciences, Keele University, Keele, Staffordshire ST55BG, UK; orcid.org/0000-0002-6775-3539; Email: m.hollamby@keele.ac.uk

Authors

Chie Otsuka – Division of Advanced Science and Engineering, Graduate School of Science and Engineering, Chiba University, Chiba 263-8522, Japan

Sho Takahashi – Division of Advanced Science and Engineering, Graduate School of Science and Engineering, Chiba University, Chiba 263-8522, Japan

Atsushi Isobe – Division of Advanced Science and Engineering, Graduate School of Science and Engineering, Chiba University, Chiba 263-8522, Japan; orcid.org/0000-0001-7567-1480

Takuho Saito – Division of Advanced Science and Engineering, Graduate School of Science and Engineering, Chiba University, Chiba 263-8522, Japan; orcid.org/0000-0002-5941-6006

Takumi Aizawa – Division of Advanced Science and Engineering, Graduate School of Science and Engineering, Chiba University, Chiba 263-8522, Japan; orcid.org/0000-0002-2285-6374

Ryoma Tsuchida – Division of Advanced Science and Engineering, Graduate School of Science and Engineering, Chiba University, Chiba 263-8522, Japan

Shuhei Yamashita – Division of Advanced Science and Engineering, Graduate School of Science and Engineering, Chiba University, Chiba 263-8522, Japan

Koji Harano – Center for Basic Research on Materials, National Institute for Materials Science, Tsukuba, 305-0044, Japan; orcid.org/0000-0001-6800-8023

Hiroki Hanayama – Division of Advanced Science and Engineering, Graduate School of Science and Engineering, Chiba University, Chiba 263-8522, Japan; orcid.org/0000-0002-6922-7620

Nobutaka Shimizu – Photon Factory, Institute of Materials Structure Science, High Energy Accelerator Research Organization, Tsukuba 305-0801, Japan; orcid.org/0000-0002-3636-1663

Hideaki Takagi – Photon Factory, Institute of Materials Structure Science, High Energy Accelerator Research Organization, Tsukuba 305-0801, Japan

Rie Haruki – Photon Factory, Institute of Materials Structure Science, High Energy Accelerator Research Organization, Tsukuba 305-0801, Japan

Luzhi Liu – School of Chemistry and Chemical Engineering, Guangxi University, Nanning, Guangxi 530004, China; orcid.org/0000-0001-9710-9624

Notes

The authors declare no competing financial interest.

ACKNOWLEDGMENTS

This work was supported by the Japan Society for the Promotion for Science (JSPS) KAKENHI grant no. 21H02038, 22H00331, 23H04874, and 23H04873 in a Grant-in-Aid for Transformative Research Areas "Materials Science of Meso-Hierarchy". S.Y. acknowledges financial support from The Mitsubishi Foundation. This work was performed under the approval of the Photon Factory Program Advisory Committee (Proposal No. 2020G567). A part of this work used computational resources of the supercomputer Fugaku provided by RIKEN through the HPCI System Research Project (Project ID: hp220405). We acknowledge the computational resources provided by the Institute of Management and Information Technologies, Chiba University.

REFERENCES

(1) Hoeben, F. J. M.; Jonkheijm, P.; Meijer, E. W.; Schenning, A. P. H. J. About Supramolecular Assemblies of π-Conjugated Systems. *Chem. Rev.* **2005**, *105*, 1491–1546.

(2) Chen, Z.; Lohr, A.; Saha-Möller, C. R.; Würthner, F. Self-Assembled π-Stacks of Functional Dyes in Solution: Structural and Thermodynamic Features. *Chem. Soc. Rev.* **2009**, *38*, 564–584.

(3) Pisula, W.; Feng, X.; Müllen, K. Tuning the Columnar Organization of Discotic Polycyclic Aromatic Hydrocarbons. *Adv. Mater.* **2010**, *22*, 3634–3649.

(4) Wu, J.; Pisula, W.; Müllen, K. Graphenes as Potential Material for Electronics. *Chem. Rev.* **2007**, *107*, 718–747.

(5) Würthner, F.; Saha-Möller, C. R.; Fimmel, B.; Ogi, S.; Leowanawat, P.; Schmidt, D. Perylene Bisimide Dye Assemblies as Archetype Functional Supramolecular Materials. *Chem. Rev.* **2016**, *116*, 962–1052.

(6) Ishiwari, F.; Shoji, Y.; Fukushima, T. Supramolecular Scaffolds Enabling the Controlled Assembly of Functional Molecular Units. *Chem. Sci.* **2018**, *9*, 2028–2041.

(7) Jelley, E. E. Spectral Absorption and Fluorescence of Dyes in the Molecular State. *Nature* **1936**, *138*, 1009–1010.

(8) Würthner, F.; Kaiser, T. E.; Saha-Möller, C. R. J-Aggregates: From Serendipitous Discovery to Supramolecular Engineering of Functional Dye Materials. *Angew. Chem. Int. Ed.* **2011**, *50*, 3376–3410.

(9) Hestand, N. J.; Spano, F. C. Expanded Theory of H- and J-Molecular Aggregates: The Effects of Vibronic Coupling and Intermolecular Charge Transfer. *Chem. Rev.* **2018**, *118*, 7069–7163.

(10) Kim, J. H.; Schembri, T.; Bialas, D.; Stolte, M.; Würthner, F. Slip-Stacked J-Aggregate Materials for Organic Solar Cells and Photodetectors. *Adv. Mater.* **2022**, *34*, 2104678.

(11) Ishii, T.; Shinkai, S. Dye-Based Organogels: Stimuli-Responsive Soft Materials Based on One-Dimensional Self-Assembling Aromatic Dyes. In *Supermolecular Dye Chemistry*; Springer-Verlag: Berlin/Heidelberg; pp 119–160.

(12) Babu, S. S.; Praveen, V. K.; Ajayaghosh, A. Functional π-Gelators and Their Applications. *Chem. Rev.* **2014**, *114*, 1973–2129.

(13) Kato, T.; Uchida, J.; Ichikawa, T.; Sakamoto, T. Functional Liquid Crystals towards the Next Generation of Materials. *Angew. Chem. Int. Ed.* **2018**, *57*, 4355–4371.

(14) Wöhrle, T.; Wurzbach, I.; Kirres, J.; Kostidou, A.; Kapernaum, N.; Litterscheidt, J.; Haenle, J. C.; Staffeld, P.; Baro, A.; Giesselmann, F.; Laschat, S. Discotic Liquid Crystals. *Chem. Rev.* **2016**, *116*, 1139–1241.

(15) Mabesoone, M. F. J.; Palmans, A. R. A.; Meijer, E. W. Solute–Solvent Interactions in Modern Physical Organic Chemistry: Supramolecular Polymers as a Muse. *J. Am. Chem. Soc.* **2020**, *142*, 19781–19798.

(16) Brunsveld, L.; Folmer, B. J. B.; Meijer, E. W.; Sijbesma, R. P. Supramolecular Polymers. *Chem. Rev.* **2001**, *101*, 4071–4098.

(17) de Greef, T. F. A.; Smulders, M. M. J.; Wolffs, M.; Schenning, A. P. H. J.; Sijbesma, R. P.; Meijer, E. W. Supramolecular Polymerization. *Chem. Rev.* **2009**, *109*, 5687–5754.

(18) Aida, T.; Meijer, E. W.; Stupp, S. I. Functional Supramolecular Polymers. *Science* **2012**, *335*, 813–817.

(19) Aida, T.; Meijer, E. W. Supramolecular Polymers – We've Come Full Circle. *Isr. J. Chem*. **2020**, *60*, 33–47.

(20) Ciferri, A. *Supramolecular Polymers*, Second ed.; CRC Press, 2005.

(21) Yang, L.; Tan, X.; Wang, Z.; Zhang, X. Supramolecular Polymers: Historical Development, Preparation, Characterization, and Functions. *Chem. Rev*. **2015**, *115*, 7196–7239.

(22) Vázquez-González, V.; Mayoral, M. J.; Chamorro, R.; Hendrix, M. M. R. M.; Voets, I. K.; González-Rodríguez, D. Noncovalent Synthesis of Self-Assembled Nanotubes through Decoupled Hierarchical Cooperative Processes. *J. Am. Chem. Soc.* **2019**, *141*, 16432–16438.

(23) Zhao, D.; Moore, J. S. Nucleation–Elongation: A Mechanism for Cooperative Supramolecular Polymerization. *Org. Biomol. Chem.* **2003**, *1*, 3471–3491.

(24) Kim, H.-J.; Lim, Y.-B.; Lee, M. Self-Assembly of Supramolecular Polymers into Tunable Helical Structures. *J. Polym. Sci. A Polym. Chem.* **2008**, *46*, 1925–1935.

(25) Praveen, V. K.; Babu, S. S.; Vijayakumar, C.; Varghese, R.; Ajayaghosh, A. Helical Supramolecular Architectures of Self-Assembled Linear π-Systems. *Bull. Chem. Soc. Jpn.* **2008**, *81*, 1196–1211.

(26) Yashima, E.; Ousaka, N.; Taura, D.; Shimomura, K.; Ikai, T.; Maeda, K. Supramolecular Helical Systems: Helical Assemblies of Small Molecules, Foldamers, and Polymers with Chiral Amplification and Their Functions. *Chem. Rev.* **2016**, *116*, 13752–13990.

(27) Nadimetla, D. N.; Al Kobaisi, M.; Bugde, S. T.; Bhosale, S. V. Tuning Achiral to Chiral Supramolecular Helical Superstructures. *Chem. Rec.* **2020**, *20*, 793–819.

(28) Sang, Y.; Liu, M. Hierarchical Self-Assembly into Chiral Nanostructures. *Chem. Sci.* **2022**, *13*, 633–656.

(29) Liu, M.; Zhang, L.; Wang, T. Supramolecular Chirality in Self-Assembled Systems. *Chem. Rev.* **2015**, *115*, 7304–7397.

(30) Oh, J. S.; Kim, K. Y.; Kim, M.; Kim, S.; Jung, S. H.; Jung, J. H. Chiral Supramolecular Multiblock Copolymerization Accompanying Chirality Transfer in Heterostructures via Living Chain Growth. *Angew. Chem. Int. Ed.* **2023**, *62*, e202300913.

(31) Tevis, I. D.; Palmer, L. C.; Herman, D. J.; Murray, I. P.; Stone, D. A.; Stupp, S. I. Self-Assembly and Orientation of Hydrogen-Bonded Oligothiophene Polymorphs at Liquid–Membrane–Liquid Interfaces. *J. Am. Chem. Soc.* **2011**, *133*, 16486–16494.

(32) Fukui, T.; Kawai, S.; Fujinuma, S.; Matsushita, Y.; Yasuda, T.; Sakurai, T.; Seki, S.; Takeuchi, M.; Sugiyasu, K. Control over Differentiation of a Metastable Supramolecular Assembly in One and Two Dimensions. *Nat. Chem.* **2017**, *9*, 493–499.

(33) Langenstroer, A.; Kartha, K. K.; Dorca, Y.; Droste, J.; Stepanenko, V.; Albuquerque, R. Q.; Hansen, M. R.; Sánchez, L.; Fernández, G. Unraveling Concomitant Packing Polymorphism in Metallosupramolecular Polymers. *J. Am. Chem. Soc.* **2019**, *141*, 5192–5200.

(34) Aizawa, T.; Aratsu, K.; Datta, S.; Mashimo, T.; Seki, T.; Kajitani, T.; Silly, F.; Yagai, S. Hydrogen Bond-Directed Supramolecular Polymorphism Leading to Soft and Hard Molecular Ordering. *Chem. Commun.* **2020**, *56*, 4280–4283.

(35) Aizawa, T.; Takahashi, S.; Isobe, A.; Datta, S.; Sotome, H.; Miyasaka, H.; Kajitani, T.; Yagai, S. Fluorescent Supramolecular Polymorphism Driven by Distinct Hydrogen Bonding Lattice. *Chem. Lett.* **2020**, *49*, 1009–1012.

(36) Pal, T.; Chaudhuri, D. Chiral and Morphological Anisotropy of Supramolecular Polymers Shaped by a Singularity in Solvent Composition. *J. Am. Chem. Soc.* **2023**, *145*, 2532–2543.

(37) Bujosa, S.; Doncel-Giménez, A.; Bäumer, N.; Fernández, G.; Ortí, E.; Costa, A.; Rotger, C.; Aragó, J.; Soberats, B. Thermoreversible Polymorph Transitions in Supramolecular Polymers of Hydrogen-Bonded Squaramides. *Angew. Chem. Int. Ed.* **2022**, *61*, e202213345.

(38) Das, G.; Cherumukkil, S.; Padmakumar, A.; Banakar, V. B.; Praveen, V. K.; Ajayaghosh, A. Tweaking a BODIPY Spherical Self-Assembly to 2D Supramolecular Polymers Facilitates Excited-State Cascade Energy Transfer. *Angew. Chem. Int. Ed.* **2021**, *60*, 7851–7859.

(39) Suda, N.; Saito, T.; Arima, H.; Yagai, S. Photo-Modulation of Supramolecular Polymorphism in the Self-Assembly of a Scissor-Shaped Azobenzene Dyad into Nanotoroids and Fibers. *Chem. Sci.* **2022**, *13*, 3249–3255.

(40) Suzuki, A.; Aratsu, K.; Datta, S.; Shimizu, N.; Takagi, H.; Haruki, R.; Adachi, S.; Hollamby, M.; Silly, F.; Yagai, S. Topological Impact on the Kinetic Stability of Supramolecular Polymers. *J. Am. Chem. Soc.* **2019**, *141*, 13196–13202.

(41) Wehner, M.; Würthner, F. Supramolecular Polymerization through Kinetic Pathway Control and Living Chain Growth. *Nat. Rev. Chem.* **2020**, *4*, 38–53.

(42) Matern, J.; Dorca, Y.; Sánchez, L.; Fernández, G. Revising Complex Supramolecular Polymerization under Kinetic and Thermodynamic Control. *Angew. Chem. Int. Ed.* **2019**, *58*, 16730–16740.

(43) Sorrenti, A.; Leira-Iglesias, J.; Markvoort, A. J.; de Greef, T. F. A.; Hermans, T. M. Non-Equilibrium Supramolecular Polymerization. *Chem. Soc. Rev.* **2017**, *46*, 5476–5490.

(44) Shen, C. A.; Bialas, D.; Hecht, M.; Stepanenko, V.; Sugiyasu, K.; Würthner, F. Polymorphism in Squaraine Dye Aggregates by Self-Assembly Pathway Differentiation: Panchromatic Tubular Dye Nanorods versus J-Aggregate Nanosheets. *Angew. Chem. Int. Ed.* **2021**, *60*, 11949–11958.

(45) Das, A.; Maity, B.; Koley, D.; Ghosh, S. Slothful Gelation of a Dipolar Building Block by "Top-down" Morphology Transition from Microparticles to Nanofibres. *Chem. Commun.* **2013**, *49*, 5757–5759.

(46) Mabesoone, M. F. J.; Markvoort, A. J.; Banno, M.; Yamaguchi, T.; Helmich, F.; Naito, Y.; Yashima, E.; Palmans, A. R. A.; Meijer, E. W. Competing Interactions in Hierarchical Porphyrin Self-Assembly Introduce Robustness in Pathway Complexity. *J. Am. Chem. Soc.* **2018**, *140*, 7810–7819.

(47) Wehner, M.; Röhr, M. I. S.; Bühler, M.; Stepanenko, V.; Wagner, W.; Würthner, F. Supramolecular Polymorphism in

One-Dimensional Self-Assembly by Kinetic Pathway Control. *J. Am. Chem. Soc.* **2019**, *141*, 6092–6107.

(48) Li, Z.; Chen, S.; Gao, C.; Yang, Z.; Shih, K. C.; Kochovski, Z.; Yang, G.; Gou, L.; Nieh, M. P.; Jiang, M.; Zhang, L.; Chen, G. Chemically Controlled Helical Polymorphism in Protein Tubes by Selective Modulation of Supramolecular Interactions. *J. Am. Chem. Soc.* **2019**, *141*, 19448–19457.

(49) Yagai, S. Supramolecularly Engineered Functional π-Assemblies Based on Complementary Hydrogen-Bonding Interactions. *Bull. Chem. Soc. Jpn.* **2015**, *88*, 28–58.

(50) Adhikari, B.; Lin, X.; Yamauchi, M.; Ouchi, H.; Aratsu, K.; Yagai, S. Hydrogen-Bonded Rosettes Comprising π-Conjugated Systems as Building Blocks for Functional One-Dimensional Assemblies. *Chem. Commun.* **2017**, *53*, 9663–9683.

(51) Prabhu, D. D.; Aratsu, K.; Kitamoto, Y.; Ouchi, H.; Ohba, T.; Hollamby, M. J.; Shimizu, N.; Takagi, H.; Haruki, R.; Adachi, S.; Yagai, S. Self-Folding of Supramolecular Polymers into Bioinspired Topology. *Sci. Adv.* **2018**, *4*. eaat8466.

(52) Isobe, A.; Prabhu, D. D.; Datta, S.; Aizawa, T.; Yagai, S. Effect of an Aromatic Solvent on Hydrogen-Bond-Directed Supramolecular Polymerization Leading to Distinct Topologies. *Chem. Eur. J.* **2020**, *26*, 8997–9004.

(53) Rosen, B. M.; Wilson, C. J.; Wilson, D. A.; Peterca, M.; Imam, M. R.; Percec, V. Dendron-Mediated Self-Assembly, Disassembly, and Self-Organization of Complex Systems. *Chem. Rev.* **2009**, *109*, 6275–6540.

(54) Yagai, S.; Kitamoto, Y.; Datta, S.; Adhikari, B. Supramolecular Polymers Capable of Controlling Their Topology. *Acc. Chem. Res.* **2019**, *52*, 1325–1335.

(55) Datta, S.; Takahashi, S.; Yagai, S. Nanoengineering of Curved Supramolecular Polymers: Toward Single-Chain Mesoscale Materials. *Acc. Mater. Res.* **2022**, *3*, 259–271.

(56) Kitamoto, Y.; Pan, Z.; Prabhu, D. D.; Isobe, A.; Ohba, T.; Shimizu, N.; Takagi, H.; Haruki, R.; Adachi, S.; Yagai, S. One-Shot Preparation of Topologically Chimeric Nanofibers via a Gradient Supramolecular Copolymerization. *Nat. Commun.* **2019**, *10*. No. 4578.

(57) Datta, S.; Kato, Y.; Higashiharaguchi, S.; Aratsu, K.; Isobe, A.; Saito, T.; Prabhu, D. D.; Kitamoto, Y.; Hollamby, M. J.; Smith, A. J.; Dagleish, R.; Mahmoudi, N.; Pesce, L.; Perego, C.; Pavan, G. M.; Yagai, S. Self-Assembled Poly-Catenanes from Supramolecular Toroidal Building Blocks. *Nature* **2020**, *583*, 400–405.

(58) MacDonald, J. C.; Whitesides, G. M. Solid-State Structures of Hydrogen-Bonded Tapes Based on Cyclic Secondary Diamides. *Chem. Rev.* **1994**, *94*, 2383–2420.

(59) Rossi, D.; Gelbrich, T.; Kahlenberg, V.; Griesser, U. J. Supramolecular Constructs and Thermodynamic Stability of Four Polymorphs and a Co-Crystal of Pentobarbital (Nembutal). *CrystEngComm* **2012**, *14*, 2494–2506.

(60) Gelbrich, T.; Meischberger, I.; Griesser, U. J. Two Polymorphs of 5-Cyclohexyl-5-Ethylbarbituric Acid and Their Packing Relationships with Other Barbiturates. *Acta Crystallogr., Sect. C: Struct. Chem.* **2015**, *71*, 204–210.

(61) Adhikari, B.; Aratsu, K.; Davis, J.; Yagai, S. Photoresponsive Circular Supramolecular Polymers: A Topological Trap and Photoinduced Ring-Opening Elongation. *Angew. Chem. Int. Ed.* **2019**, *58*, 3764–3768.

(62) Smulders, M. M. J.; Nieuwenhuizen, M. M. L.; de Greef, T. F. A.; van der Schoot, P.; Schenning, A. P. H. J.; Meijer, E. W. How to Distinguish Isodesmic from Cooperative Supramolecular Polymerisation. *Chem. Eur. J.* **2010**, *16*, 362–367.

(63) Kaiser, T. E.; Stepanenko, V.; Würthner, F. Fluorescent J-Aggregates of Core-Substituted Perylene Bisimides: Studies on Structure-Property Relationship, Nucleation-Elongation Mechanism, and Sergeants-and-Soldiers Principle. *J. Am. Chem. Soc.* **2009**, *131*, 6719–6732.

(64) Yagai, S.; Usui, M.; Seki, T.; Murayama, H.; Kikkawa, Y.; Uemura, S.; Karatsu, T.; Kitamura, A.; Asano, A.; Seki, S. Supramolecularly Engineered Perylene Bisimide Assemblies Exhibiting Thermal Transition from Columnar to Multilamellar Structures. *J. Am. Chem. Soc.* **2012**, *134*, 7983–7994.

(65) van der Zwaag, D.; Pieters, P. A.; Korevaar, P. A.; Markvoort, A. J.; Spiering, A. J. H.; de Greef, T. F. A.; Meijer, E. W. Kinetic Analysis as a Tool to Distinguish Pathway Complexity in Molecular Assembly: An Unexpected Outcome of Structures in Competition. *J. Am. Chem. Soc.* **2015**, *137*, 12677–12688.

(66) Korevaar, P. A.; George, S. J.; Markvoort, A. J.; Smulders, M. M. J.; Hilbers, P. A. J.; Schenning, A. P. H. J.; de Greef, T. F. A.; Meijer, E. W. Pathway Complexity in Supramolecular Polymerization. *Nature* **2012**, *481*, 492–496.

(67) Xu, J.; Zhou, H.; Yu, Q.; Guerin, G.; Manners, I.; Winnik, M. A. Synergistic Self-Seeding in One-Dimension: A Route to Patchy and Block Comicelles with Uniform and Controllable Length. *Chem. Sci.* **2019**, *10*, 2280–2284.

(68) Choi, I.; Kang, S. Y.; Yang, S.; Yun, N.; Choi, T. L. Fabrication of Semiconducting Nanoribbons with Tunable Length and Width via Crystallization-Driven Self-Assembly of a Homopolymer Prepared by Cyclopolymerization Using Grubbs Catalyst. *Macromolecules* **2022**, *55*, 3484–3492.

(69) Qian, J.; Lu, Y.; Cambridge, G.; Guerin, G.; Manners, I.; Winnik, M. A. Polyferrocenylsilane Crystals in Nanoconfinement: Fragmentation, Dissolution, and Regrowth of Cylindrical Block Copolymer Micelles with a Crystalline Core. *Macromolecules* **2012**, *45*, 8363–8372.

(70) Schnitzer, T.; Preuss, M. D.; van Basten, J.; Schoenmakers, S. M. C.; Spiering, A. J. H.; Vantomme, G.; Meijer, E. W. How Subtle Changes Can Make a Difference: Reproducibility in Complex Supramolecular Systems. *Angew. Chem. Int. Ed.* **2022**, *61*, e202206738.

(71) Adhikari, B.; Yamada, Y.; Yamauchi, M.; Wakita, K.; Lin, X.; Aratsu, K.; Ohba, T.; Karatsu, T.; Hollamby, M. J.; Shimizu, N.; Takagi, H.; Haruki, R.; Adachi, S.; Yagai, S. Light-Induced Unfolding and Refolding of Supramolecular Polymer Nanofibres. *Nat. Commun.* **2017**, *8*. No.15254.

(72) Hollamby, M. J.; Aratsu, K.; Pauw, B. R.; Rogers, S. E.; Smith, A. J.; Yamauchi, M.; Lin, X.; Yagai, S. Simultaneous SAXS and SANS Analysis for the Detection of Toroidal Supramolecular Polymers Composed of Noncovalent Supermacrocycles in Solution. *Angew. Chem. Int. Ed.* **2016**, *55*, 9890-9893.

(73) Aratsu, K.; Takeya, R.; Pauw, B. R.; Hollamby, M. J.; Kitamoto, Y.; Shimizu, N.; Takagi, H.; Haruki, R.; Adachi, S.; Yagai, S. Supramolecular Copolymerization Driven by Integrative Self-Sorting of Hydrogen-Bonded Rosettes. *Nat. Commun.* **2020**, *11,* No. 1623.

(74) Xu, F.; Crespi, S.; Pacella, G.; Fu, Y.; Stuart, M. C. A.; Zhang, Q.; Portale, G.; Feringa, B. L. Dynamic Control of a Multistate

Chiral Supramolecular Polymer in Water. *J. Am. Chem. Soc.* **2022**, *144*, 6019–6027.

(75) Breßler, I.; Kohlbrecher, J.; Thünemann, A. F. SASfit: A Tool for Small-Angle Scattering Data Analysis Using a Library of Analytical Expressions. *J. Appl. Crystallogr.* **2015**, *48*, 1587–1598.

(76) Xing, J.; Takeuchi, K.; Kamei, K.; Nakamuro, T.; Harano, K.; Nakamura, E. Atomic-Number (*Z*)-Correlated Atomic Sizes for Deciphering Electron Microscopic Molecular Images. *Proc. Natl. Acad. Sci. U. S. A.* **2022**, *119*, e2114432119.

(77) Itoh, Y.; Chen, S.; Hirahara, R.; Konda, T.; Aoki, T.; Ueda, T.; Shimada, I.; Cannon, J. J.; Shao, C.; Shiomi, J.; Tabata, K. V.; Noji, H.; Sato, K.; Aida, T. Ultrafast Water Permeation through Nanochannels with a Densely Fluorous Interior Surface. *Science* **2022**, *376*, 738–743.

(78) Shen, B.; Zhu, Y.; Kim, Y.; Zhou, X.; Sun, H.; Lu, Z.; Lee, M. Autonomous Helical Propagation of Active Toroids with Mechanical Action. *Nat. Commun.* **2019**, *10*, 1080.

Table of Contents artwork